Automated Quantitative Assessment of Coronary Calcification Using Intravascular Ultrasound

Liu, Shengnan; Neleman, Tara; Hartman, Eline M.J.; Ligthart, Jurgen M.R.; Witberg, Karen T.; van der Steen, Antonius F.W.; Wentzel, Jolanda J.; Daemen, Joost; van Soest, Gijs

DOI
10.1016/j.ultrasmedbio.2020.04.032

Publication date
2020

Document Version
Final published version

Published in
Ultrasound in Medicine and Biology

Ultrasound in Med. & Biol., Vol. 00, No. 00, pp. 1–9, 2020

0301-5629/$ - see front matter

https://doi.org/10.1016/j.ultrasmedbio.2020.04.032

● *Original Contribution*

AUTOMATED QUANTITATIVE ASSESSMENT OF CORONARY CALCIFICATION USING INTRAVASCULAR ULTRASOUND

Shengnan Liu,* Tara Neleman,* Eline M.J. Hartman,* Jurgen M.R. Ligthart,* Karen T. Witberg,* Antonius F.W. van der Steen,*,†,‡ Jolanda J. Wentzel,* Joost Daemen,* and Gijs van Soest*

* Department of Cardiology, Erasmus University Medical Center, Rotterdam, The Netherlands; † Department of Imaging Physics, Faculty of Applied Sciences, Delft University of Technology, The Netherlands; and ‡ Shenzhen Institutes of Advanced Technologies, Shenzhen, China

Abstract—Coronary calcification represents a challenge in the treatment of coronary artery disease by stent placement. It negatively affects stent expansion and has been related to future adverse cardiac events. Intravascular ultrasound (IVUS) is known for its high sensitivity in detecting coronary calcification. At present, automated quantification of calcium as detected by IVUS is not available. For this reason, we developed and validated an optimized framework for accurate automated detection and quantification of calcified plaque in coronary atherosclerosis as seen by IVUS. Calcified lesions were detected by training a supported vector classifier per IVUS A-line on manually annotated IVUS images, followed by post-processing using regional information. We applied our framework to 35 IVUS pullbacks from each of the three commonly used IVUS systems. Cross-validation accuracy for each system was >0.9, and the testing accuracy was 0.87, 0.89 and 0.89 for the three systems. Using the detection result, we propose an IVUS calcium score, based on the fraction of calcium-positive A-lines in a pullback segment, to quantify the extent of calcified plaque. The high accuracy of the proposed classifier suggests that it may provide a robust and accurate tool to assess the presence and amount of coronary calcification and, thus, may play a role in image-guided coronary interventions. (E-mail: g.vansoest@erasmusmc.nl) **© 2020 The Author(s). Published by Elsevier Inc. on behalf of World Federation for Ultrasound in Medicine & Biology. This is an open access article under the CC BY license. (http://creativecommons.org/licenses/by/4.0/).**

Key Words: **Calcified plaque, Intravascular ultrasound, Automated quantification, Intravascular imaging, Coronary artery disease.**

INTRODUCTION

Coronary artery disease, the most common heart disease, is caused by a long-term accumulation of atherosclerotic plaque in the intima of the arterial vessel wall (Falk 2006; Hong 2010). As plaques grow, they may impinge on the free coronary lumen, causing a stenosis that limits blood flow to the myocardial territory served by the coronary artery. Severe or acute coronary artery disease is frequently treated by stent implantation in a procedure called percutaneous coronary intervention (PCI). Atherosclerotic plaques are frequently heterogeneous in their composition, and typically consist of fibrous, lipid-rich and calcified tissue.

The presence of calcium, in particular, can hamper the feasibility of PCI (Hoffmann et al. 1998). Because of its rigidity, circumferential calcification may prevent full dilation of the stent, which may lead to stent underexpansion, associated with increased risk of target vessel failure (Witzenbichler et al. 2014). Specialized techniques, such as cutting balloons, rotational atherectomy or intracoronary lithotripsy (Sharma et al. 2019), can be used to prepare calcified plaques to enable complete stent expansion. The beneficial effects of these plaque modification techniques depend directly on the extent and severity of calcification, so detailed knowledge is needed to guide the choice of lesion preparation method (Wijns et al. 2015).

Large calcified plaques can often be unambiguously identified in intravascular ultrasound (IVUS) images because of their high reflection of and low penetration by ultrasound signals (Pu et al. 2014; Mintz and Guagliumi 2017). As illustrated in Figure 1, coronary calcium is characterized as a narrow band with high echo intensities, with a dark shadow behind it. Current IVUS software does not allow automated calcium quantification.

Address correspondence to: Gijs van Soest, PO Box 2040, 3000 CA Rotterdam, The Netherlands. E-mail: g.vansoest@erasmusmc.nl

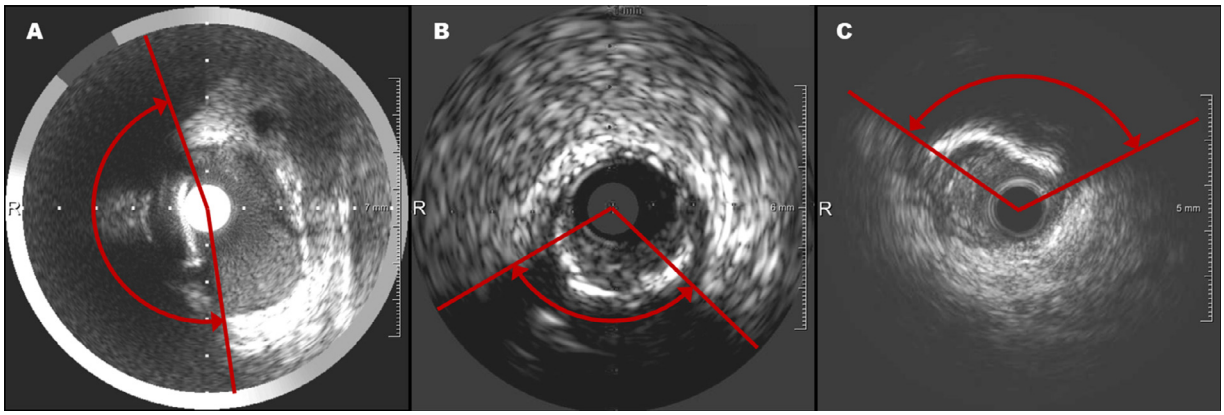

Fig. 1. Three images in gray scale from Infraredx (a), Volcano (b) and Boston Scientific (c). The calcified plaque is marked with a *red arch*.

Because of the presence of inherent speckle, various system- and anatomy-dependent artifacts, limited resolution and image contrast, automated structure detection in IVUS remains a challenging task (Katouzian et al. 2012). Simple approaches, using thresholding (Kim et al. 2014) and adaptive thresholding, have been reported (Dos Santos Filho et al. 2007). A more complex approach to segmentation of the leading edge of calcified plaque combining Rayleigh mixture models, Markov random fields, graph searching and prior knowledge, has been reported (Gao et al. 2014). After detection of the intima and the media–adventitia borders, calcified regions were detected using a Bayesian classifier (Taki et al. 2008). Two recent studies have reported the detection of calcification per frame using a deep learning network (Balocco et al. 2018; Sofian et al. 2018).

In this work, we present a framework for accurate automated detection and quantification of the extent of calcification in coronary atherosclerosis as seen by IVUS. Without multistep pre-processing, extraction of complex features or design of a deep learning approach to perform the task, we found that accurate classification can be achieved by applying a kernel-based support vector classifier on simple statistical features, originating from the imaging physics, extracted directly from un-processed images. Using data from three commonly used IVUS systems, we trained the classifier for recognition of calcified plaques per A-line. Using the detection result, we propose an IVUS calcium score (ICS) to evaluate the calcified plaque load and compare it with the calcium score based on manual labels.

METHODS

IVUS data

IVUS pullback data sets, acquired in native coronary arteries, were extracted from the clinical database of the Department of Cardiology, Erasmus MC. The data sets were anonymized and contained no identifying information; all selected patients consented to the use of their data in retrospective studies. All data in this study were collected as part of routine clinical care. Consequently, institutional review board approval and individual patient consent are not required under Dutch law. We selected 105 pullbacks, 35 each from three commonly used systems: Infraredx (40 MHz, TVC NIRS Catheter System, Infraredx Inc., Burlington, MA, USA), Volcano (20 MHz, Eagle Eye Platinum Rx, and ST Rx, Digital IVUS Catheters, Volcano Corp., Rancho Cordova, CA, USA) and Boston Scientific (40 MHz, Atlatis SR Pro and OptiCross Coronary Imaging Catheter, Boston Scientific Corp., Natick, MA, USA). Example images from the three systems are provided in Figure 1.

An overview is given in Table 1. Pullbacks, stored in DICOM format, were manually annotated by trained experts (E.M.J.H. and T.N.) at 1-mm intervals. Centering at the imaging catheter, we divided and labeled each frame as a calcified or non-calcified pie sector (Fig. 2).

Table 1. Data description

Vendor	Population	Pullback	Frame rate (fs/s)	Pullback speed (mm/s)	Training	Test
Infraredx	34	35	16	0.5	31	4
Volcano	35	35	30	0.5	31	4
Boston Scientific	35	35	30	0.5	31	4

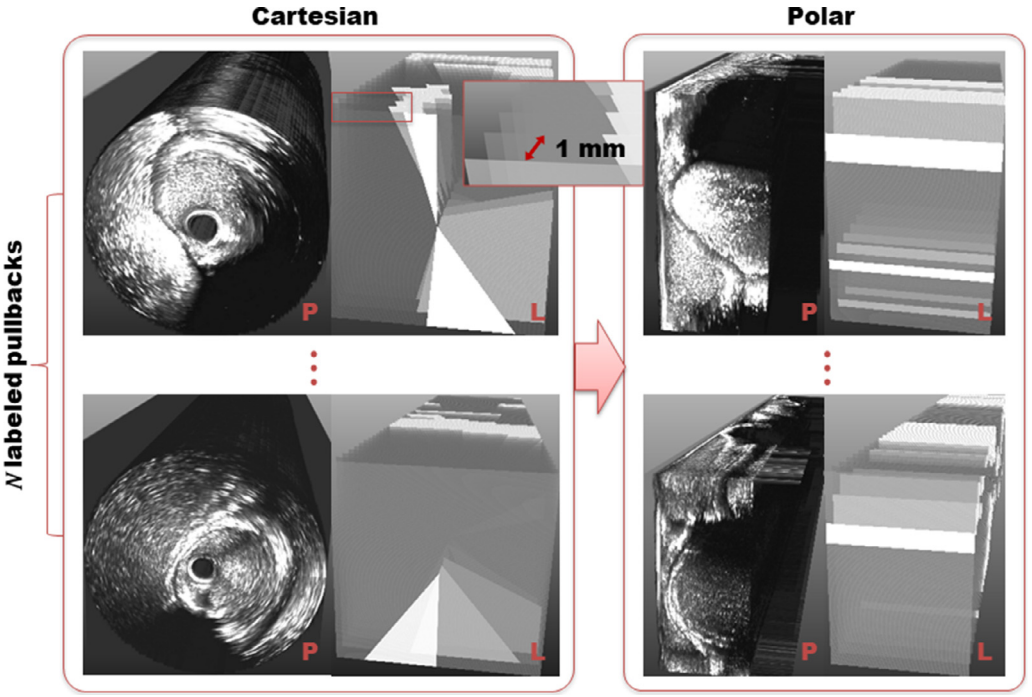

Fig. 2. Pullback stacks were labeled in Cartesian coordinates and converted to polar coordinates. 'P' marks the pullbacks, and 'L' marks the label stack. In the zoomed-in *red rectangular box*, a scale bar is given indicating the pullbacks were labeled every 1 mm. The labeled stacks in the right panels are shown with transparency.

Frames (in Cartesian coordinates) and their corresponding labels were converted into polar coordinates, such that each A-line was binary labeled as 1 (calcified) or 0 (non-calcified).

Identifying features

Calcified plaque can be confidently classified by human observers. The A-line profile itself is quite variable though, within each (calcified or non-calcified) category. By comparing the A-line amplitude statistics, we observed that the typical combination of a thin reflection and dorsal shadow of calcium in IVUS may be used as a discriminating characteristic, whereas an A-line scan of soft tissue contains many gray values and most amplitude values in a line sampling calcium are low (lumen and shadow), with a few very high ones (calcium border). To build an unbiased classifier, we decided to train it upon a rich feature set, including 10 distribution densities, 10 distribution quantiles and the mean value (21 in total; examples for calcified and non-calcified A-lines are illustrated in Fig. 3).

Training the detection model

We trained a radial basis function (RBF) support vector classification (SVC) model to classify IVUS A-lines. An SVC is a flexible structure used to classify high-dimensional data. A basic trained SVC is a linear hyperplane, which can separate only linearly separable clusters. To deal with data that are not linearly separable, a non-linear kernel needs to be introduced. When little is known about the structure of data, a Gaussian RBF kernel is a robust choice, assuming only general smoothness (Smola and Schölkopf 2004).

Each A-line is characterized by a set of statistical features x_i,and has a binary label y_i identifying it as calcified or not. For M labeled A-line distributions, $\{(x_i, y_i)|\ y_i \in \{0, 1\}, i \in \{0, \cdots, M\}\}$, a classifier

$$f(x) = \mathrm{sgn}\left[\sum_{i=1}^{n} \alpha_i y_i K(x_i, x) + b\right]$$

was trained to optimize the problem (Guyon et al. 1993)

$$\min_\alpha \frac{1}{2}\alpha^T Q\alpha - e^T\alpha \ \text{ such that } y^T\alpha = 0,\quad 0 \le \alpha_i \le C, i = 1, \cdots, n \tag{1}$$

Here, e is a vector of ones, and C is a parameter balancing the complexity and training error to be tolerated. Q is a $n \times n$ positive semidefinite matrix, and $Q_{ij} \equiv y_i y_j K(x_i, x_j)$ and $K(x_i, x_j) = \exp(\| -x_i - x_j \|^2 / 2\sigma^2)$ is the commonly used Gaussian RBF kernel. σ governs the linearity of the classifier: larger σ values allow greater nonlinearity. The hyperparameters C and σ were determined by an exhaustive grid search optimizing overall classification performance.

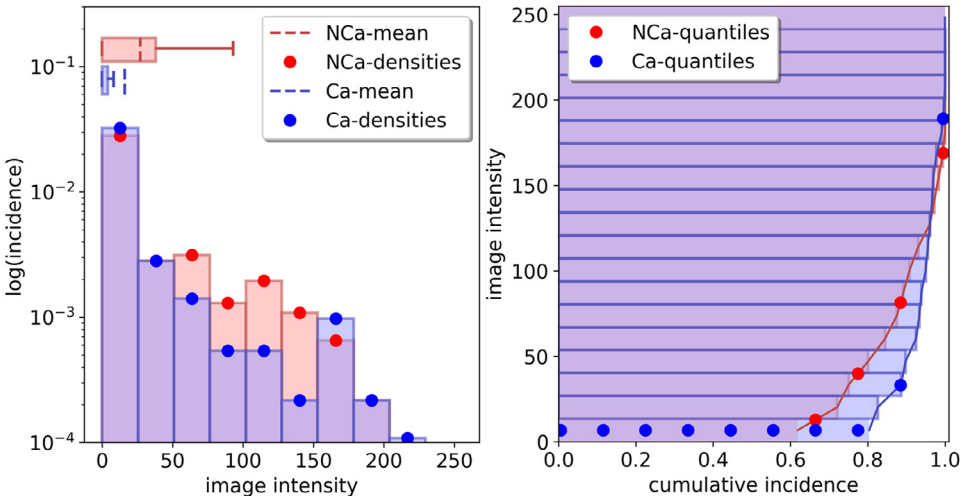

Fig. 3. Features extracted from image intensities, depicting an example of a calcified A-line (*blue*) and a non-calcified A-line (red) from the manually annotated set. The mean value and the distribution densities are given in the left panel, and the quantiles, in the right panel.

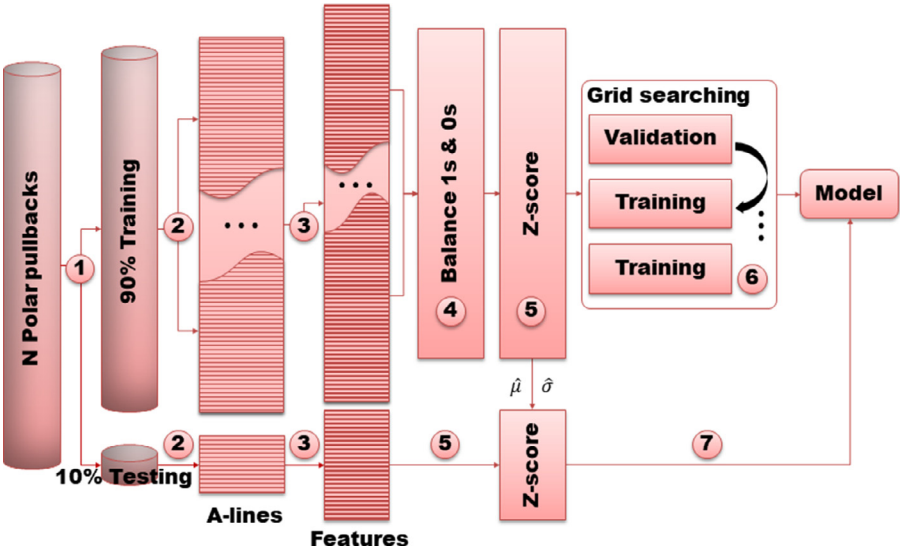

Fig. 4. Flowchart for training the support vector machine. The numbered steps are explained in the text under Training the Detection Model.

Table 2. Overview of performance of support vector machine

Vendor	Experiment	Measurement			
		Accuracy*	Precision	Recall	F1 score
Infraredx	Training	0.9170 ± 0.0003	0.95	0.91	0.93
	Testing	0.87	0.96	0.77	0.86
Volcano	Training	0.9113 ± 0.0002	0.92	0.93	0.92
	Testing	0.89	0.89	0.90	0.89
Boston Scientific	Training	0.9084 ± 0.0004	0.92	0.91	0.92
	Testing	0.89	0.92	0.85	0.88

* For training we report the cross-validation accuracy.

Figure 4 is the flowchart for model training and testing; the numbered steps are as follows:

Step 1. The pullbacks in polar coordinates were randomly split 9:1; 90% were used for training and 10% were used for testing. The splitting numbers of pullbacks for each system are given in Table 2.

Step 2. After generating the training and testing data set, we extracted the image gray values for each A-line in the labeled frames.

Step 3. The distribution densities were calculated by generating a histogram of the image gray values in [0; 255] in 10 bins. They were normalized such that the sum is 1. The 10 quantiles were linearly sampled in the range 0.5%−99.5%.

Step 4. Because there were more non-calcified than calcified A-lines, we balanced the training categories by randomly downsampling the non-calcified A-lines such that the total number of non-calcified A-lines was equal to that of calcified A-lines.

Step 5. The input was further normalized using *Z*-score normalization. The estimated mean $(\hat{\mu})$ and the standard deviation $(\hat{\sigma})$ were derived from the training set and later applied to *Z*-score normalize the testing set.

Step 6. Hyperparameters C and σ were selected. Grid points were evenly chosen on a double log scale, $\{C_i = 10^{u_i} | u_i \in [-3, 3], i = 1, \cdots, \mathrm{M}\} \times \{$ $\sigma_j = 10^{\upsilon_j} | \upsilon_j \in [-5, 3], j = 1, \cdots, \mathrm{N}\}$; $M = N = 21$. The A-lines were randomized in the ratio 3:7 to training and validation sets for threefold cross-validation. The parameters with the highest accuracy were chosen for use in the final model. We find that there is a large range with nearly optimal performance for $\sigma \in [10^{-4}, 10^{-1}]$, approximately, with minimal effect of the value of C, indicating limited sensitivity to algorithm or data specifics.

Step 7. The final trained model was applied to the testing data. Precision, recall and the F1 score, given in eqn (2), were computed on balanced data where the negative examples were downsampled to be equal to the amount of positive examples.

Post-processing

After performing the classification, we applied the dense fully connected conditional random field (CRF) as the post-processing for noise removal (Krähenbühl and Koltun 2011). The method applies a Gaussian penalty when two pixels in the defined neighborhood have different labels. In combination of prior probability, the *a posteriori* probability was maximized with an optimized labeling solution. Here the prior probability was estimated for each pullback using the SVC-detected label, and the neighborhood was empirically chosen to be 10 frames and 21 A-lines. Followed by an in-frame morphological closing (1×21) and opening (1×51), the post-processing steps remove isolated positive and negative classifications and integrate labels with small gaps.

Validation and reporting

The model was trained for each system separately. Performance in the testing set was evaluated in the number of true/false positive/negative (TP, TN, FP, FN) A-line classifications, and reported in precision, recall and F1 score (Fawcett 2006):

$$\begin{aligned} \text{precision} &= \frac{\mathrm{TP}}{\mathrm{TP} + \mathrm{FP}} \\ \text{recall} &= \frac{\mathrm{TP}}{\mathrm{TP} + \mathrm{FP}} \end{aligned} \tag{2}$$

$$\text{F1 score} = 2 \cdot \frac{\text{precision} \cdot \text{recall}}{\text{precision} + \text{recall}}$$

For further validation, we introduced the ICS, which is defined as the fraction of detected calcified A-lines in the total acquired number. Two ICSs were calculated using labeled frames; one was estimated using the manual labels (denoted as s) and the other was estimated using the detection results (denoted as $\hat{s}$):

$$s = \frac{\#(\text{labeled calcified A}-\text{lines})}{\#(\text{all A}-\text{lines})} \text{ in all labeled frames}$$

$$\hat{s} = \frac{\#(\text{detected calcified A}-\text{lines})}{\#(\text{all A}-\text{lines})} \text{ in all labeled frames}$$

During the comparison we observed that s and $\hat{s}$ are linearly related to each other. Therefore, we applied the random sample consensus (RANSAC) regression to highlight outliers and to fit a linear function $(\hat{s} = ks + b)$ with inliers. Outliers were removed before computing Pearson's correlation coefficient:

$$r_{xy} = \frac{n\sum x_i y_i - \sum x_i \sum y_i}{\sqrt{n\sum x_i^2 (\sum x_i)^2}\sqrt{n\sum y_i^2 - (\sum y_i)^2}}, \quad \text{for } i \in \{0, 1, \cdots, \mathrm{n}\}$$

We further adjusted the detected values by applying the linear transform $f(\hat{s}) = (\hat{s} - b)/k$.

Using the estimation result on a whole pullback, we then calculated a total ICS (denoted as $\hat{s}_{\text{total}}$), which can give an overall indication of the amount of calcified plaque in the whole pullback.

$$\hat{s}_{\text{total}} = \frac{\#(\text{detected calcified A}-\text{lines})}{\#(\text{all A}-\text{lines})}$$

Furthermore, similar to intravascular near-infrared spectroscopy (Gardner et al. 2008), we present a local ICS (denoted as $\hat{s}_M$) in short segments, for instance, 2 mm, which can intuitively highlight artery sections with a heavy calcium burden:

$$\hat{s}_M = \frac{\#(\text{detected calcified A}-\text{lines})}{\#(\text{all A}-\text{lines})} \text{ in } M \text{ neighboring frames}$$

Again inspired by previous work on IVUS palpography (Schaar et al. 2004) and parametric intravascular optical coherence tomography (Gnanadesigan et al. 2016), we represent the detection result in a so-called "carpet view", depicting the classification result in a display with dimensions of circumferential angle and pullback length.

RESULTS

Table 2 summarizes the overall performance of A-line-based calcium detection by the support vector machine (SVM) trained on the data. We observe that an average accuracy >0.9 was achieved, with small variations across validation experiments and similarly high in testing sets. The manual ICS s and the detected ICS $\hat{s}$ are compared in scatterplots in Figure 5. Despite a moderate overestimation, the two numbers are highly correlated (Infraredx: $r = 0{:}94$, Volcano: $r = 0{:}88$, Boston Scientific: $r = 0{:}97$). The Wilcoxon tests suggest that the manual and automated measurements are sampled from the same distribution (Infraredx: $p = 0.6138$, Volcano: $p = 0.9426$, Boston Scientific: $p = 0.8370$).

A carpet view representation of the calcium detection results is provided in Figure 6. *White areas* indicate calcification. *Vertical lines* represent manually labeled frames, where red and blue designate calcium-positive and calcium-negative A-lines, respectively. The color bar above the carpet view displays the local ICS calculated every 2 mm. The local ICS provides an intuitive overview of the distribution of calcified plaques, with circumferential calcium ($s_{2\text{mm}} = 1000$) occurring in Figure 6a and b.

DISCUSSION

In the present study, we developed a pipeline for automated detection of calcified plaque on IVUS images. Using an SVC classifier and CRF post-processing, we attempted to use simple statistical features of image intensities for an A-line-based identification of calcium in the arterial wall. Results indicate that the proposed framework can be used for a robust estimation of an IVUS-based calcium score, which can be used as an objective evaluation of the presence and amount of calcified plaque in the vessel, overall and locally.

ICS overestimates calcium in specific situations

In total, 16 pullbacks were detected as outliers (Infraredx: 9, Volcano: 6, Boston Scientific: 1), 15 of which are overestimations comparing with the manual scores. All outliers were part of the training set. If the outliers had arisen in testing data, they could be indicative of overfitting. Rather, *post hoc* examination suggested that the overestimation occurred mainly in three scenarios.

First, some non-calcium image features cannot be distinguished from calcium features, based on A-line intensity statistics only. When the pericardial cavity is visible in the IVUS image, it appears as a thin bright band (visceral pericardium) followed by an abrupt dark cavity. This structure usually appears in large series of consecutive frames and can lead to massive overestimation. This was observed in three arteries and, in one case, was observed in 4264 of 5281 frames in one pullback. Occasionally, when large arteries are imaged with an eccentric catheter, leaving only a bright band of signals on the far wall, the statistical features can be similar to those from calcified regions. This was observed in five arteries.

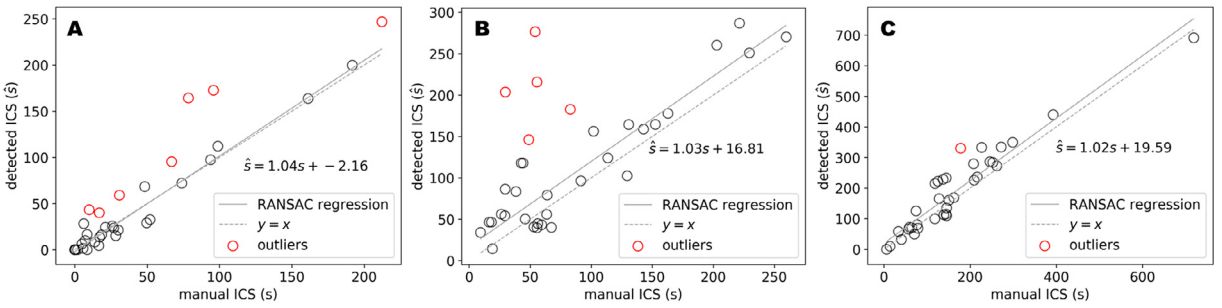

Fig. 5. Scatterplot of ground-truth intravascular ultrasound calcium score (ICS) calculated using manual labels (s) and the ICS calculated using the detected labels ($\hat{s}$), acquired with the three different intravascular ultrasound systems: (a) Infraredx, (b) Volcano, (c) Boston Scientific. RANSAC = random sample consensus.

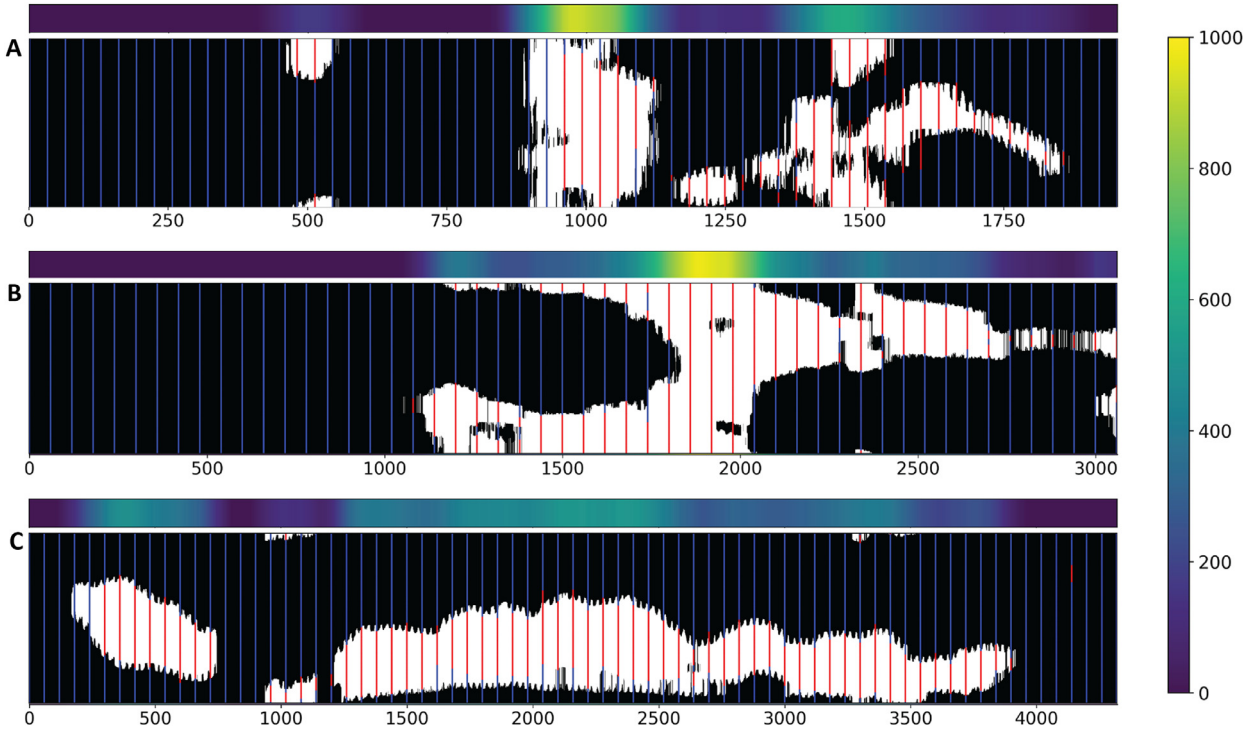

Fig. 6. Detection results in carpet views (circumferential angle × frame number), where detected calcified regions are in *white* and non-calcified regions are in *black*. Positive manual labels are represented by *red lines*, and the negative counterparts, by *blue lines*. The colored strip above each carpet view represents the local intravascular ultrasound calcium score (2 mm windows), ranging from 0 to 1000 (colorbar on the right). Examples from three different systems: (a) Infraredx, (b) Volcano, (c) Boston Scientific.

Second, post-processing is designed to remove small positive regions (which are likely to be false). False positives that are adjacent to a lesion are difficult to rule out, however. This may cause structures such as the guidewire to be classified as calcium.

Third, calcified regions appearing as a bright band, with a dorsal shadow, are relatively easy to identify for the experts. However, some calcified plaques exhibit normal brightness with dark shadows (in the case of a directional reflection from a non-normal surface not received by the transducer). The correct classification of this appearance of calcified plaque requires the observation of several neighboring frames, which were not available to the experts in this study. Compared with the experts' labels, the detection framework performs more consistently for the detection of ''dark'' calcified lesions. However, in our reporting this is counted as an overestimation when compared with the experts' labels.

Comparison with previous work

The present approach differs in a number of ways from recent work, which employed deep learning frameworks (Balocco et al. 2018; Sofian et al. 2018). First, we employed data from three different IVUS systems and developed a universally applicable analysis that differs only in the weights of the SVM. Second, our analysis did not require pre-processing (motion correction, gating, conversion to polar coordinates). This formulation of the calcium detection problem, which respects the independence of A-lines and relies on statistical features in the data that result directly from the imaging physics, outperforms the convolutional neural network-based classifier described by Balocco et al. (2018) as measured by the F1 score. Sofian et al. (2018) analyzed only isolated, selected frames, which are not necessarily representative of clinical data.

Outlook on application: Clinical research

For analysis of large intravascular imaging data sets, algorithmic quantification of plaque features can accelerate quantification studies by eliminating the time-consuming manual annotation of thousands of images, while simultaneously improving reproducibility and reducing inter-observer variation. Future work, including prospective studies, will be needed to evaluate the value of the ICS for stratification of the risk of follow-up events after the index PCI.

For asymptomatic populations, the relation between calcified atherosclerosis and cardiovascular events has been quantified in the coronary artery calcium score, an

important non-invasive diagnostic metric used to predict cardiac risk with computed tomography (CT) (Shah and Coulter 2012). CT detects calcified plaque with high accuracy, with a systematic overestimation of the plaque volume (Leber et al. 2006; Sun et al. 2008; Voros et al. 2011). CT lacks sensitivity to small calcifications compared with IVUS (Van Der Giessen et al. 2011). In our study, no such independent assessment of coronary calcium was available. As a result, the ICS has not been validated as a measure of the true amount of calcification in a vessel.

Outlook on application: Intervention guidance

Operator experience plays an important role in the practical use and utility of IVUS in PCI. Automated image analysis can be helpful for the development of objective and fast IVUS-guided PCI strategies. Many studies have found that imaging techniques can effectively reduce periprocedural (Witzenbichler et al. 2014; Zhang et al. 2018) and late ischemic events (Di Mario et al. 2018). Robust, real-time automated detection of plaque features can make the technology easier to use and thus more accessible.

Observational studies reported that calcified lesions can be associated with post-PCI adverse events, including restenosis and stent thrombosis (Witzenbichler et al. 2014). Moderate and severe calcifications were associated with major adverse events and revascularization in the target artery observed in the 3 years after the implantation of a stent (Shiode et al. 2018). Untreated calcified lesions may also trigger later adverse cardiac events (Mintz 2015). Exposed calcified nodules have been identified as a substrate for thrombus formation, leading to acute coronary syndrome (Virmani et al. 2000; Jia et al. 2013).

We introduced here a local measure of the calcium burden, by computing the ICS in short (2-mm) segments. In the future, the ICS may serve to indicate heavily calcified regions that may be likely to benefit from lesion preparation during PCI. A threshold value of the ICS for intervention guidance remains to be determined in follow-up research.

CONCLUSIONS

We presented an optimized framework for accurate automated detection and quantification of the presence and extent of calcification in coronary atherosclerosis as seen by IVUS. Calcified lesions were detected by training a support vector classifier per IVUS A-line on manually annotated pullback data, followed by post-processing using regional information.

With manual annotations as a standard, an overall accuracy of $\sim 0{:}9$ was achieved. Based on this classifier, we proposed an ICS that comprehensively characterizes the extent of coronary calcification in a vessel examined by IVUS.

Conflict of interest disclosure—The authors have no conflicts of interest to declare.

REFERENCES

Balocco S, González M, Ñanculef R, Radeva P, Thomas G. Calcified plaque detection in IVUS sequences: Preliminary results using convolutional nets. In: Hernández Heredia Y, Milián Núñez V, Ruiz Shulcloper J, (eds). Progress in Artificial Intelligence and Pattern Recognition, IWAIPR 2018. Lecture Notes in Computer Science. 11047, Cham: Springer; 2018. p. 34–42.

Di Mario C, Koskinas KC, Räber L. Clinical benefit of IVUS guidance for coronary stenting. J Am Coll Cardiol 2018;72:3138–3141.

Dos Santos Filho E, Saijo Y, Tanaka A, Yambe T, Li S, Yoshizawa M. Automated calcification detection and quantification in intravascular ultrasound images by adaptive thresholding. In: Magjarevic R, Nagel JH, (eds). World Congress on Medical Physics and Biomedical Engineering 2006. IFMBE Proceedings, Vol. 14. Berlin/Heidelberg. : Springer Verlag; 2007. p. 1421–1425.

Falk E. Pathogenesis of atherosclerosis. J Am Coll Cardiol 2006;47: C7–C12.

Fawcett T. An introduction to ROC analysis. Pattern Recognit Lett 2006;27:861–874.

Gao Z, Guo W, Liu X, Huang W, Zhang H, Tan N, Hau WK, Zhang YT, Liu H. Automated detection framework of the calcified plaque with acoustic shadowing in IVUS images. PLoS One 2014;9 e109997.

Gardner CM, Tan H, Hull EL, Lisauskas JB, Sum ST, Meese TM, Jiang C, Madden SP, Caplan JD, Burke AP, Virmani R, Goldstein J, Muller JE. Detection of lipid core coronary plaques in autopsy specimens with a novel catheter-based near-infrared spectroscopy system. JACC Cardiovasc Imaging 2008;1:638–648.

Gnanadesigan M, Kameyama T, Karanasos A, Van Ditzhuijzen NS, Van Der Sijde JN, Van Geuns RJ, Ligthart J, Witberg K, Ughi GJ, Van Der Steen AF, Regar E, Van Soest G. Automated characterisation of lipid core plaques in vivo by quantitative optical coherence tomography tissue type imaging. EuroIntervention 2016;12: 1490–1497.

Guyon I, Boser BE, Vapnik V. Automatic capacity tuning of very large VC-dimension classifiers. In: Hanson SJ, Cowan JD, Giles CL, (eds). Advances in neural information processing systems 5 (NIPS Conference). San Francisco. : Morgan Kaufmann; 1993. p. 147–155.

Hoffmann R, Mintz GS, Popma JJ, Satler LF, Kent KM, Pichard AD, Leon MB. Treatment of calcified coronary lesions with Palmaz-Schatz stents: An intravascular ultrasound study. Eur Heart J 1998;19:1224–1231.

Hong YM. Atherosclerotic cardiovascular disease beginning in childhood. Korean Circ J 2010;40:1.

Jia H, Abtahian F, Aguirre AD, Lee S, Chia S, Lowe H, Kato K, Yonetsu T, Vergallo R, Hu S, Tian J, Lee H, Park SJ, Jang YS, Raffel OC, Mizuno K, Uemura S, Itoh T, Kakuta T, Choi SY, Dauerman HL, Prasad A, Toma C, McNulty I, Zhang S, Yu B, Fuster V, Narula J, Virmani R, Jang IK. In vivo diagnosis of plaque erosion and calcified nodule in patients with acute coronary syndrome by intravascular optical coherence tomography. J Am Coll Cardiol 2013;62:1748–1758.

Katouzian A, Angelini ED, Carlier SG, Suri JS, Navab N, Laine AF. A state-of-the-art review on segmentation algorithms in intravascular ultrasound (IVUS) images. IEEE Trans Inf Technol Biomed 2012;16:823–834.

Kim SW, Mintz GS, Lee WS, Cho JH, Hong SA, Kwon JE, Lee TJ, Park ES, Park KS, Hong JH, Seok JW, Cha YJ, Kim HJ, Kim CJ, Kim TH. DICOM based intravascular ultrasound signal intensity analysis: An echoplaque medical imaging bench study. Coron Artery Dis 2014;25:236–241.

Krähenbühl P, Koltun V. Efficient inference in fully connected CRFs with gaussian edge potentials. In: Shawe-Taylor J, Zemel RS, Bartlett PL, Pereira F, Weinberger KQ, (eds). Advances in neural information processing systems 24. Red Hook, NY: Curran Associates; 2011. p. 109–117.

Leber AW, Becker A, Knez A, Von Ziegler F, Sirol M, Nikolaou K, Ohnesorge B, Fayad ZA, Becker CR, Reiser M, Steinbeck G, Boekstegers P. Accuracy of 64-slice computed tomography to classify and quantify plaque volumes in the proximal coronary system: A comparative study using intravascular ultrasound. J Am Coll Cardiol 2006;47:672–677.

Mintz GS. Intravascular imaging of coronary calcification and its clinical implications. JACC Cardiovasc Imaging 2015;8:461–471.

Mintz GS, Guagliumi G. Intravascular imaging in coronary artery disease. Lancet 2017;390:793–809.

Pu J, Mintz GS, Biro S, Lee JB, Sum ST, Madden SP, Burke AP, Zhang P, He B, Goldstein JA, Stone GW, Muller JE, Virmani R, Maehara A. Insights into echo-attenuated plaques, echolucent plaques, and plaques with spotty calcification: Novel findings from comparisons among intravascular ultrasound, near-infrared spectroscopy, and pathological histology in 2,294 human coronary artery segments. J Am Coll Cardiol 2014;63:2220–2233.

Schaar JA, Regar E, Mastik F, McFadden EP, Saia F, Disco C, de Korte CL, de Feyter PJ, van der Steen AFW, Serruys PW. Incidence of high-strain patterns in human coronary arteries: Assessment with three-dimensional intravascular palpography and correlation with clinical presentation. Circulation 2004;109:2716–2719.

Shah NR, Coulter SA. An evidence-based guide for coronary calcium scoring in asymptomatic patients without coronary heart disease. Tex Hear Inst J 2012;39:240–242.

Sharma SK, Tomey MI, Teirstein PS, Kini AS, Reitman AB, Lee AC, Généreux P, Chambers JW, Grines CL, Himmelstein SI, Thompson CA, Meredith IT, Bhave A, Moses JW. North American expert review of rotational atherectomy. Circ Cardiovasc Interv 2019;12 e007448.

Shiode N, Kozuma K, Aoki J, Awata M, Nanasato M, Tanabe K, Yamaguchi J, Kusano H, Nie H, Kimura T. The impact of coronary calcification on angiographic and 3-year clinical outcomes of everolimus-eluting stents: Results of a XIENCE V/PROMUS post-marketing surveillance study. Cardiovasc Interv Ther 2018;33:313–320.

Smola AJ, Schölkopf B. A tutorial on support vector regression. Stat Comput 2004;14:199–222.

Sofian H, Chia Ming JT, Mohamad S, Noor NM. Calcification detection using deep structured learning in intravascular ultrasound image for coronary artery disease. 2018 2nd International Conference on BioSignal Analysis, Processing and Systems (ICBAPS 2018), Kuching, Malaysia. Piscataway, NJ. : IEEE; 2018. p. 47–52.

Sun J, Zhang Z, Lu B, Yu W, Yang Y, Zhou Y, Wang Y, Fan Z. Identification and quantification of coronary atherosclerotic plaques: A comparison of 64-MDCT and intravascular ultrasound. Am J Roentgenol 2008;190:748–754.

Taki A, Najafi Z, Roodaki A, Setarehdan SK, Zoroofi RA, Konig A, Navab N. Automatic segmentation of calcified plaques and vessel borders in IVUS images. Int J Comput Assist Radiol Surg 2008;3:347–354.

Van Der Giessen AG, Gijsen FJ, Wentzel JJ, Jairam PM, Van Walsum T, Neefjes LA, Mollet NR, Niessen WJ, Van De Vosse FN, De Feyter PJ, Van Der Steen AF. Small coronary calcifications are not detectable by 64-slice contrast enhanced computed tomography. Int J Cardiovasc Imaging 2011;27:143–152.

Virmani R, Kolodgie FD, Burke AP, Farb A, Schwartz SM. Lessons from sudden coronary death. Arterioscler Thromb Vasc Biol 2000;20:1262–1275.

Voros S, Rinehart S, Qian Z, Vazquez G, Anderson H, Murrieta L, Wilmer C, Carlson H, Taylor K, Ballard W, Karmpaliotis D, Kalynych A, Brown C. Prospective validation of standardized, 3-dimensional, quantitative coronary computed tomographic plaque measurements using radiofrequency backscatter intravascular ultrasound as reference standard in intermediate coronary arterial lesions. JACC Cardiovasc Interv 2011;4:198–208.

Wijns W, Shite J, Jones MR, Lee SWL, Price MJ, Fabbiocchi F, Barbato E, Akasaka T, Bezerra H, Holmes D. Optical coherence tomography imaging during percutaneous coronary intervention impacts physician decision making: ILUMIEN I study. Eur Heart J 2015;36:3346–3355.

Witzenbichler B, Maehara A, Weisz G, Neumann FJ, Rinaldi MJ, Metzger DC, Henry TD, Cox DA, Duffy PL, Brodie BR, Stuckey TD, Mazzaferri EL, Xu K, Parise H, Mehran R, Mintz GS, Stone GW. Relationship between intravascular ultrasound guidance and clinical outcomes after drug-eluting stents: The assessment of dual antiplatelet therapy with drug-eluting stents (ADAPT-DES) study. Circulation 2014;129:463–470.

Zhang J, Gao X, Kan J, Ge Z, Han L, Lu S, Tian N, Lin S, Lu Q, Wu X, Li Q, Liu Z, Chen Y, Qian X, Wang J, Chai D, Chen C, Li X, Gogas BD, Pan T, Shan S, Ye F, Chen SL. Intravascular ultrasound versus angiography guided drug-eluting stent implantation: The ULTIMATE trial. J Am Coll Cardiol 2018;72:3126–3137.